



# Winter precipitation particle size distribution measurement by Multi-Angle Snowflake Camera



Gwo-Jong Huang\*, Cameron Kleinkort, V.N. Bringi, Branislav M. Notaroš

Colorado State University, Fort Collins, CO, United States

## A B S T R A C T

From the radar meteorology viewpoint, the most important properties for quantitative precipitation estimation of winter events are 3D shape, size, and mass of precipitation particles, as well as the particle size distribution (PSD). In order to measure these properties precisely, optical instruments may be the best choice. The Multi-Angle Snowflake Camera (MASC) is a relatively new instrument equipped with three high-resolution cameras to capture the winter precipitation particle images from three non-parallel angles, in addition to measuring the particle fall speed using two pairs of infrared motion sensors. However, the results from the MASC so far are usually presented as monthly or seasonally, and particle sizes are given as histograms, no previous studies have used the MASC for a single storm study, and no researchers use MASC to measure the PSD. We propose the methodology for obtaining the winter precipitation PSD measured by the MASC, and present and discuss the development, implementation, and application of the new technique for PSD computation based on MASC images. Overall, this is the first study of the MASC-based PSD. We present PSD MASC experiments and results for segments of two snow events to demonstrate the performance of our PSD algorithm. The results show that the self-consistency of the MASC measured single-camera PSDs is good. To cross-validate PSD measurements, we compare MASC mean PSD (averaged over three cameras) with the collocated 2D Video Disdrometer, and observe good agreements of the two sets of results.

## 1. Introduction

The quantitative precipitation estimation (QPE) using operational weather radar is very important for winter weather forecasting, hydrology, detection of aviation hazards and other remote sensing applications (e.g., ground validation for microwave radiometry from space). It is not difficult to measure the liquid equivalent snow rate (henceforth snow rate or SR) by using snow gauges such as a heating bucket snow gauge, Geonor or Pluvio. The biggest challenge for an accurate QPE by the radar comes from the interaction between the radar electromagnetic wave and precipitation, and thus the relationship between the radar scattering measurement and precipitation observation, due to the variety and variability of winter precipitation particle microphysical properties which, in addition, can change dramatically with, for example, relatively small changes in environmental conditions (Magono and Lee, 1966; Pruppacher and Klett, 1978). These important micro-physical properties include but are not limited to the shape, density (or mass), characteristic dimension (or size), and particle size distribution (PSD). Two components of the radar-based QPE for a winter event are the radar measurements and SR, and the most

commonly used relationship between the two components is the equivalent reflectivity factor ( $Z_e$ ) and SR power law relationship. The most direct method to derive the  $Z_e$ -SR relationship is to correlate  $Z_e$  from the radar and SR measured by a gauge (Fujiyoshi et al., 1990 and references therein). Due to the spatial and temporal decorrelation, this method could lead to large uncertainties. The other method which can reduce these uncertainties is based on the use of a ground disdrometer (i.e., Two-Dimensional Video Disdrometer, 2DVD; Schönhuber et al., 2000) to measure the PSD, and evaluate or assume the precipitation particle mass, and then derive the  $Z_e$  and SR.

Previous studies show that if mass-size and fall speed-size power laws can be estimated (e.g., Matrosov et al., 2009) or pre-assumed and the PSD is measured (e.g., Sekhon and Srivastava, 1970), the  $Z_e$  can be derived by integrating mass square over the PSD (Ryzhkov et al., 1998) and SR is the fall speed multiplied by the mass and integrated over the PSD. Huang et al. (2010) used 2DVD measured PSD, and adjusted the coefficient and exponent of a pre-assumed density-size power law relation to fit the 2DVD derived  $Z_e$  with King City radar measured  $Z_r$ . This “effective” density was applied to the 2DVD PSD to compute the 2DVD SR, which, in turn, was compared with a Geonor snow gauge, and a

\* Corresponding author at: Colorado State University, Department of Electrical and Computer Engineering, 1373 Campus Delivery, Fort Collins, CO 80523, United States.  
E-mail address: [Gwo-Jong.Huang@colostate.edu](mailto:Gwo-Jong.Huang@colostate.edu) (G.-J. Huang).

good agreement of these two SRs was observed. Böhm (1989, 1992), Heymsfield et al. (2004), and Heymsfield and Westbrook (2010) showed that one can compute fall speed from mass based on aerodynamics' principle. Huang et al. (2015) inverted their fall speed-mass relation to compute the winter precipitation particle mass (or density) on a particle-by-particle basis using a 2DVD. Fitting these particle-by-particle masses and sizes, they estimated a density (mass) to size power law relation. Applying this relation, they were then able to obtain the 2DVD derived  $Z_e$  and SR, and further to estimate a  $Z_e$ -SR relationship. Their study shows that the  $Z_e$ -SR relationship derived from a ground disdrometer can reduce the bias of the accumulated SR significantly as compared with a climatological  $Z_e$ -SR when applied to the operational radar.

There are two key parameters essential for a better estimation of the density or mass of a winter precipitation particle by using aerodynamics principles, particle shape and fall speed. In order to obtain the particle shape, the optical disdrometer is the best choice. There are a number of optical disdrometers in addition to the 2DVD. A similar research instrument to the 2DVD is a HVSD (Hydrometeor Velocity Size Detector; Barthazy et al., 2004), which measures the fall speed in two parallel optical planes. Since its two line scan cameras are looking into the same direction at different heights, the HVSD measured fall speed is very reliable and the image distortion due to the horizontal movement of a particle can be corrected easily. In contrary, it only captures the particle image in one view and it is insufficient for an irregularly shaped object. Other research instruments are the Snow Video Imager (SVI; Newman et al., 2009) and its advanced version, Precipitation Imaging Package (PIP; Liao et al., 2016), which, unlike the line scan camera, use a CCD (Charge-Coupled Device) full frame camera (60 frames per second for SVI and 360 frames per second for PIP) and images are obtained almost simultaneously. The advantages of the SVI (or PIP) are that it has a large sample volume (at least twice that of the 2DVD) so that the measured PSD will have a smaller sampling error, and better pixel resolution (nominally 0.2 mm by 0.2 mm).

All the ground based optical disdrometers outlined above capture the particle three-dimensional (3D) shape and project it to one vertical plane (HVSD, SVI and PIP) or two vertical planes (2DVD). The most important 2D projection of a hydrometeor shape for the mass estimation is the 3D-shape projected on the horizontal plane because it is the plane against the air flow (Böhm, 1989). However, it is not realistic to place a camera on the bottom of the disdrometer to look vertically. The other possible method to get the 2D-shape projection on the horizontal plane is based on using multiple 2D-shape images to reconstruct a 3D-shape. This method requires at least two non-parallel 2D-shape images, but more different at-angle images are necessary to be able to obtain a more realistic and accurate 3D-shape reconstruction. The Multi-Angle Snowflake Camera (MASC; Garrett et al., 2012) is a relatively new instrument equipped with three high-resolution cameras to capture the winter precipitation particle images from three non-parallel angles. The high-resolution images along with an extremely short exposure time (40  $\mu$ s) are ensuring that a very fine detail of the particle can be captured and that the image is not sensitive to particle velocity. Moreover, the MASC is also equipped with two pairs of infrared motion sensors to measure the fall speed of a precipitation particle. These features make the MASC a powerful tool to study the microphysical properties of winter precipitation.

However, to the best of our knowledge, the MASC manufacturer has not developed the algorithms to compute the PSD of precipitation based on the MASC measurements, and such algorithms have not been addressed in the literature either. The few previous studies use the MASC to classify the snow types, obtain the fall speed and particle size (usually show the histogram). The pictures (photographs) taken by the MASC usually contain more than one snowflake (in  $\sim$ 30–70% cases) and only one fall speed is measured per a set of pictures. Therefore, users usually do not use those pictures that contain more than one clear particle image. The results from the MASC are usually presented as

monthly or seasonally. As far as we know, no previous studies have used the MASC for a single storm study and no one uses MASC to measure the PSD. In this paper, we propose the methodology for computing the winter precipitation PSD based on the MASC images, and present and discuss the development, implementation, and application of the novel technique. Overall, this is the first study of the MASC PSD.

This article is organized as follows. In Section 2, we give a brief overview of the original design of the MASC, as well as of the Colorado State University (CSU) improved version of the MASC, and explain the lens and camera selection criteria. Section 3 explains the basic idea of the PSD measurement using camera-based instruments, and proposes and explains the method and procedure for computing the PSD using MASC images. It also shows how to obtain some necessary parameters used in PSD computation, such as the observation and measurement volumes of the MASC, and describes a depth-of-field experiment designed as a principal component of the proposed PSD evaluation method. It presents as well an image processing method to measure the size of particles from MASC photographs. In Section 4, we elaborate on the PSD MASC computation based on the uniform size bin width of 0.25 mm and 15-minute averaged PSDs. Segments of two cases from the MASCRAD (MASC + Radar) Project (Notaroš et al., 2016), the 26 December 2014 and 21 February 2015 snow events, to demonstrate the performance of our PSD algorithm are presented in Section 5, which discusses in detail the PSD MASC experiments and results. This section also shows that the self-consistency of the MASC measured PSD is good, and, to cross-validate PSD measurements, it further compares MASC mean PSD (average over three cameras) with the collocated 2DVD, with good observed agreements as well. Section 6 gives the conclusions and future work.

## 2. Multi-Angle Snowflake Camera

### 2.1. Original MASC

The Multi-Angle Snowflake Camera (MASC) is a relatively new instrument designed to capture high-resolution winter hydrometeor photographs from different angles. It was designed and developed at the University of Utah, and is commercially available from Fallgatter Technologies (Garrett et al., 2012). This instrument is equipped with three Unibrain Firewire-800 industrial digital cameras. This series of cameras includes four models which have different resolutions. Three cameras are aligned in the same horizontal plane and are placed around a 20-cm (diameter, i.e., distance between the opposite plates) black regular decagonal ring, with adjacent cameras being separated by 36° and all three cameras covering 72° angle in the plane (see Fig. 1). All cameras and LED flash lights (on the top of cameras) are adjusted to focus at the center of the decagonal ring. So the focus distance of each camera is slightly larger than 10 cm. To measure the fall speed of a precipitation particle, two pairs (detector and emitter) of infrared (IR) motion sensors are placed aside of the cameras (see the bottom-left panel of Fig. 1) and separated by 32 mm vertically. When an object touches the upper IR sensor area (yellow area in the bottom-left panel of Fig. 1), the microprocessor inside the MASC starts to count the time. After this object touches the bottom IR sensor area, the micro-processor triggers all cameras and computes the fall speed (by dividing the vertical distance, 32 mm, by the time) simultaneously. The photographs of all cameras are saved in JPEG format and sent to a computer through a firewire line (IEEE-1394). All of the software controlled camera parameters, such as trigger mode, camera resolution mode, and so on, are stored in the computer and communicated to the MASC microprocessor via USB-RS232.

The cameras and lenses used in the MASC can be customized as long as the selected models can fit in the MASC casing. The main considered characteristics are the picture (photograph) resolution and the area of observation. Generally speaking, a shorter focus length lens will have

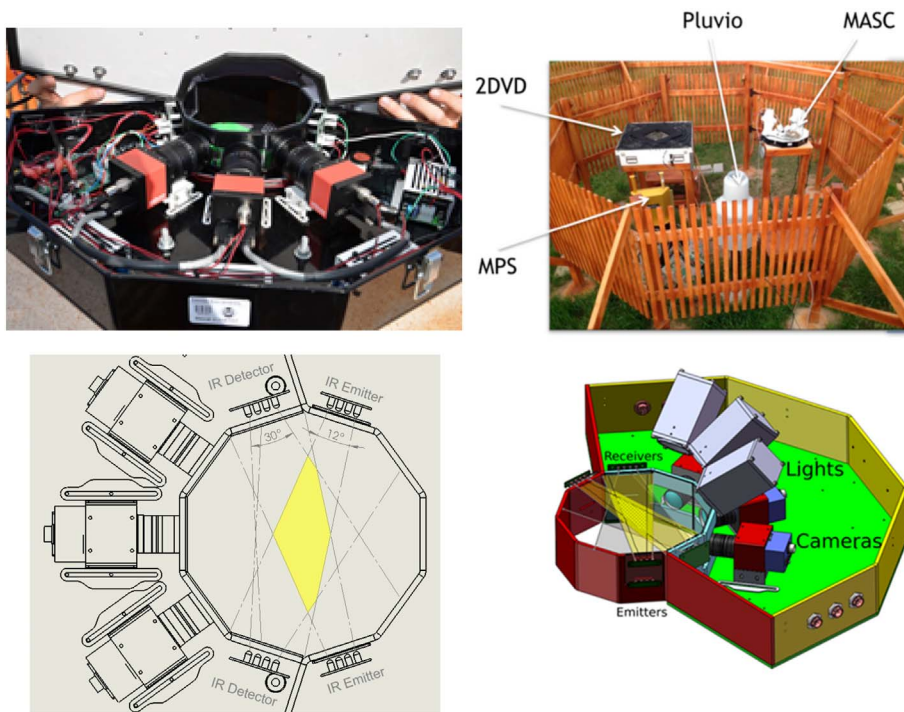


Fig. 1. (upper-left panel) Multi-Angle Snowflake Camera (MASC) – a photograph showing the MASC interior. (bottom-left panel) The top view of the MASC prototype design, where the double circle markers show the location of two IR detectors, with respective IR emitters being on the opposite sides. (upper-right panel) The instrument layout at the MASCRAD test site, near Greeley, Colorado, which included a 2/3 scale double fence intercomparison reference (DFIR) wind screen housing a MASC, 2DVD, and several other instruments. (bottom-right panel) A rough 3-dimensional sketch showing the structure of the MASC, with the three LED flash lights mounted on the top of the three original MASC cameras.

larger observation area. In tradeoff, it will reduce the image resolution and increase the distortion on the edge of the image. With the same optical-electronic technology, higher resolution requires a larger image sensor. It also means that one needs a larger camera, and it may not fit into the MASC casing. Although the larger image sensor can yield a larger observation area with the same lens, it also requires more illumination. Therefore, we may need either a longer exposure time or larger aperture (smaller  $f$  number of the lens). The longer exposure time can cause blurred image due to particle movement, and the larger aperture also blurs the image when the particle deviates from the focus plane. The users of the MASC can select the proper cameras and lenses depending on their needs.

## 2.2. CSU improved version of the MASC

Balancing two desired characteristics, a sufficient observation area to reduce the PSD sampling error and a sufficient resolution to capture the detail of a precipitation particle, CSU MASC uses Fire-i 980b with Fujinon HF12.5SA-1 12.5 mm lens for all three cameras. Fire-i 980b uses a 2/3" monochrome CCD image sensor. The highest resolution mode is  $2448 \times 2048$  pixels, or, in metric units,  $3.45 \mu\text{m} \times 3.45 \mu\text{m}$ , for CCD. When an object is located at 10 cm from the center of the 12.5-mm lens, the image resolution is 27.6 mm/pixel. This number is calculated by using pinhole camera model. The shutter rate is from  $5 \mu\text{s}$  to 3600 s. The shutter rate is set to  $40 \mu\text{s}$  and the aperture is set to  $f5.6$  according to the manufacturer's suggestion. The frame rate of this camera can be as high as 25 frames per second. Because of the bandwidth of the firewire line (IEEE-1394b), the frame rate is set to 2 frames per second per camera.

In order to acquire more images for 3D-reconstruction of particles, we have added two more camera sets (camera and lens) to the CSU MASC (Notaroš et al., 2016; Kleinkort et al., 2016). These two extra cameras use Fire-i 785b ( $1280 \times 960$  pixels) with 12.5 mm lens and are placed above the IR emitters (see the bottom panel of Fig. 1) at  $\sim 55^\circ$  with respect to the horizontal plane of the three original cameras. This setup enables more geometrical information of precipitation particles as they fall through the MASC (Kleinkort et al., 2016). However, to the best of our knowledge, all available, currently deployed and used,

MASC instruments, other than the CSU version, as well as those being produced, delivered, and planned for future users, contain three cameras. Therefore, for the generality of the approach and usefulness of the algorithm and results, in this paper our method is developed for the MASC system using the original three cameras only, with angular separation of  $36^\circ$  in one (horizontal) plane (Fig. 1).

## 3. Measurement of the PSD using MASC images

The targets of meteorological radar are precipitation particles whose sizes are, of course, much smaller than the radar resolution volume. This means that each resolution volume contains a vast number of particles. So, the best way to describe the "dimension" of targets is the size distribution. The basic form of the particle size distribution (PSD) is:

$$N(D) = N_t \cdot p(D) \quad (1)$$

where  $N_t$  is the total number (count) of particles in the volume and  $p(D)$  is a probability density function (pdf). If we sort all particles into  $N$  size bins, treat them as a discrete distribution, and consider the duration time of counting particles, Eq. (1) can be written as:

$$N(D_i) = \frac{1}{\Delta t} \sum_{k=1}^M \frac{1}{V_k \Delta D_i} \quad [\# \text{ m}^{-3} \text{ mm}^{-1}] \quad (2)$$

where  $D_i$  is the center value of the  $i^{\text{th}}$  size bin (in the units of mm),  $M$  is the number of particles in the  $i^{\text{th}}$  size bin,  $V_k$  is the measurement volume of the  $k^{\text{th}}$  particle per unit time (in the units of  $\text{m}^3 \text{ s}^{-1}$ ),  $\Delta D_i$  is the width of the  $i^{\text{th}}$  size bin (in mm), and  $\Delta t$  is the duration time (in seconds). Eq. (2) is a general equation for any camera-based optical disdrometer. Using this equation, each camera of the MASC can be viewed as a small version of the SVI, and the three cameras look at the approximately same observation volume. The main difference between the MASC and the SVI, in addition to the specifications of lenses and cameras, is that the SVI has higher frame rate, of 60 frames per second, which is constant as compared to the MASC frame rate which is maximum 2 frames per second and depends on when the IR detector is triggered (the MASC is not taking pictures constantly). Hence the key point of the MASC-based estimation of the PSD is how to find out the total measurement

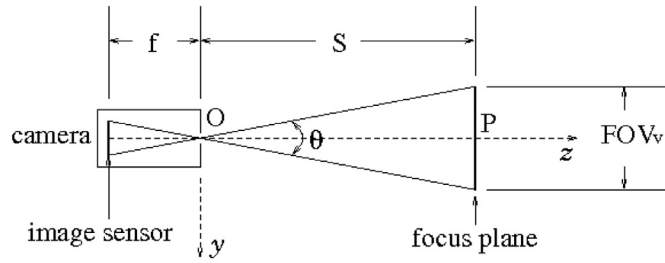


Fig. 2. “Pinhole” camera model. “O” is the center of the lens and “P” is the point at which the lens focuses.  $f$  is the focus length of the lens and  $S$  is the focus distance.  $\theta$  is the vertical angle of view (AOV).

volume during the observation time,  $V_t$  in Eq. (2).

### 3.1. Observation and measurement volumes of the MASC

The observation volume of a camera we refer to here is a 3D region for which any object located inside it can be clearly seen in a picture (photograph). Such volume of any camera can be computed using the focus length of the lens, the angle of view (AOV), the focus distance, and the depth of field (DOF). The focus distance is counted from the lens to the focus plane which can be adjusted by the lens. In our case, all three MASC cameras are adjusted to focus at the center of the decagonal ring, where the camera-to-common focal center distance is about 10 cm. The AOV can be found from the lens specifications provided by the manufacturer or computed by using “pinhole” camera model shown in Fig. 2. For example, the vertical AOV of Fujinon HF12.5SA-1 12.5 mm lens with 2/3" CCD in the manufacturer's data sheet is  $29^\circ 35'$ . Since the size of a 2/3" CCD is 8.8 mm by 6.6 mm, we can also compute the vertical AOV as  $\theta = 2 \times \tan^{-1}(6.6/2/12.5)$ , which gives the same result as above. Using the AOV and a measured focus distance ( $S$  in Fig. 2), the horizontal field of view (FOV) and vertical FOV ( $FOV_{h,v}$ ; also see Fig. 2) can be obtained easily. Then, the observation volume of any camera is:

$$V_{\text{observation}} = FOV_h \times FOV_v \times DOF \quad (3)$$

Note that, by using Eq. (3), we are assuming that the focus plane is far away from the center of lens, which means that  $S \gg f$  in Fig. 2.

The measurement volume of a camera is similar to its observation volume but is modified by the particle size because of edge particles. The edge particles are defined as those particles whose images show in the picture partially. Because of only a part of the particle image being in the picture, the sizes of those particles cannot be computed. Therefore, the edge particles should not be counted when computing the PSD. Assuming that the height of the picture is  $FOV_v$ , in order to show the whole particle of height  $H$  inside the picture, any part of the particle image must deviate from the picture edge for at least one pixel width, and hence the active  $FOV_v$  reduces to:

$$\text{active } FOV_v = FOV_v - H - 2^*p_v \quad (4)$$

where  $p_v$  is the vertical pixel width of the picture. The pixel width is given by:

$$p_{h,v} = \frac{FOV_{h,v}}{P_{h,v}} \quad (5)$$

where  $P_{h,v}$  is the horizontal (or vertical) resolution of the picture in pixels; in CSU MASC, it is 2448 (horizontal) by 2048 (vertical). Finally, the measurement volume is found as:

$$V_{\text{measurement}} = \text{active } FOV_h \times \text{active } FOV_v \times \text{applicable DOF} \quad (6)$$

It is difficult to adjust the DOF according to the particle size because it is impossible to compute the size of the particle along the optical direction ( $z$  direction in Fig. 2) by taking a 2D picture. The applicable DOF in Eq. (6) is slightly different than the theoretical DOF, as will be

explained in the next section.

### 3.2. DOF experiment

Depth of field is the range of distances for which the object falling in it can be clearly (with no blur) shown/seen in the photograph. From the geometrical optics viewpoint, only the object in the focus plane can be completely in focus in the photograph. This means that a point object in the focus plane appears as a point on the image sensor. When this point object deviates from the focus plane, the projection on image sensor will enlarge as a spot whose shape is the same as the aperture. When the diameter of this spot is larger than a pixel, it is out of focus. The distance between the nearest (with respect to the lens) and farthest non-blurry points is the DOF. The theoretical DOF can be computed from the focus length (12.5 mm), CCD size (2/3"), focus distance ( $\sim 10$  cm), and lens aperture (f5.6) (Larmore, 1965; Ray, 2002), and for the CSU MASC, it comes out to be 13.4 mm. The camera acts similarly to a human eye, and because of the perspective effect, the object near the camera has a large image in the picture. In order to accurately compute the particle size from the picture, we need to adjust the focus distance and measure the distance on a particle-by-particle basis. Even with an unlimited budget and the use of the most advance technology to achieve this goal, the measurement volume will be very small to ensure only a non-blurry particle in each picture. As a result, the sampling error of the PSD will be very high. In our case, the camera focuses at the center of the 10 cm in radius decagonal ring and does not change during the storm event. The focus distance is 10 cm plus the gap between the ring and the lens. The picture resolution of the CSU MASC is  $\sim 30 \mu\text{m}$  per pixel in the focus plane. The applicable DOF we need is defined as the range of distances where the particle falling inside can be identified as a clear image and the error of the size estimation is within  $\pm 5\%$  by our image processing code.

To evaluate the applicable DOF, we design a DOF experiment. We perform this experiment for the central camera in the set of the three original CSU MASC cameras because the three cameras are identical. The experimental procedure is the following:

1. Prepare seven black boards and print one white solid circle on each board. The white circle diameters are 1 mm, 2 mm, ..., 7 mm, respectively, for the seven boards.
2. Put a ruler on the MASC decagonal ring along the optical direction of the camera. Set the MASC to the manual trigger mode.
3. Place the black board in front of the camera. The distances from the board to the ring edge are varied from 2 cm to 17 cm with 1-cm steps for all boards except the first one, the board with a 1-mm white circle, where the image is too small to be seen when the distance is shorter than 4 cm.
4. At each distance, get 10 pictures for each board.
5. Run the image processing code without blur examination to compute the diameter, intensity, and axis ratio of the white circle from each picture.

The reason for skipping the blur examination is in that this examination procedure is designed for 3D objects with a non-smooth surface, whereas the white circle on the black board is a 2D object with a smooth surface. Moreover, we also need to estimate the diameters from those unfocused pictures.

Fig. 3 shows three pictures of the black board with the 3-mm white circle placed at distances of 8 cm, 10 cm, and 12 cm, respectively, from the edge of the MASC decagonal ring. It is obvious that the board at the 10-cm distance has the clearest image, and this is because it is actually located inside the theoretical DOF. The MASC images are in the scale of gray, with the image intensity on the scale being expressed as an integer between 0 (darkest) and 255 (brightest). We compute the mean intensity of the white circle in each picture, and then average such intensity over 10 pictures at the same distance. Fig. 4 shows the

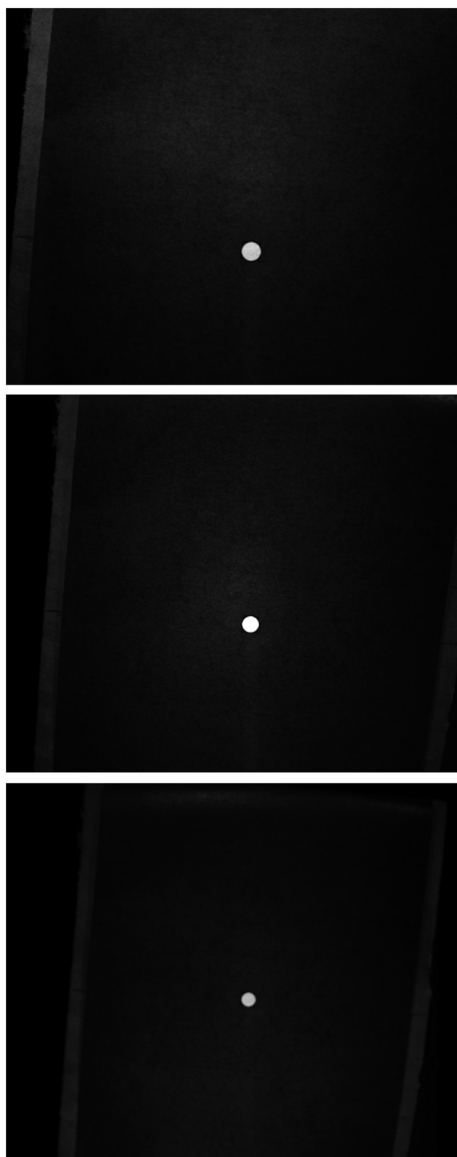


Fig. 3. MASC pictures (photographs) from the DOF (depth of field) experiment, for the white solid circle 3 mm in diameter and three distances of the black board from the edge of the MASC decagonal ring: 8 cm (top panel), 10 cm (middle panel), and 12 cm (bottom panel).

normalized averaged mean intensity versus distance. As expected, the highest value is at 9–11 cm, and there are two reasons for this result, as follows. 1) Three flash lights aim to the center of the decagonal ring, so the object in the DOF gains more illumination. 2) The area of a blurry image is enlarged in the picture, and hence the same amount of illumination spreads on a larger area on CCD causing a reduction in the image intensity. This result is important for the blur examination process because, on average, blurred images have lower intensity that tends to be smoothed out. The mean and the standard deviation of the circle axis ratio versus distance are shown in Fig. 5, where we can see that the axis ratio for different circle sizes is independent of the distance and very close to unity. The means of axis ratios are in between 0.95 and 1.05 except for the 1-mm circle. Finally, Fig. 6 shows the relative error of the mean estimated circle diameter versus the distance, with the relative error defined as:

$$Error [\%] = 100 \frac{D_{est} - D_{true}}{D_{true}} \tag{7}$$

When the circle is close to the camera, the diameter will be

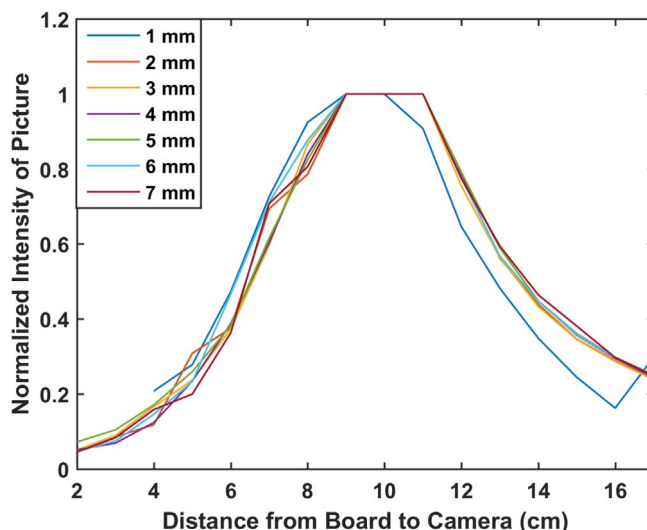


Fig. 4. Normalized averaged mean intensity of white circle images versus distance in the DOF experiment. The line colors represent different white circle diameters. The highest value is at distances from 9 cm to 11 cm.

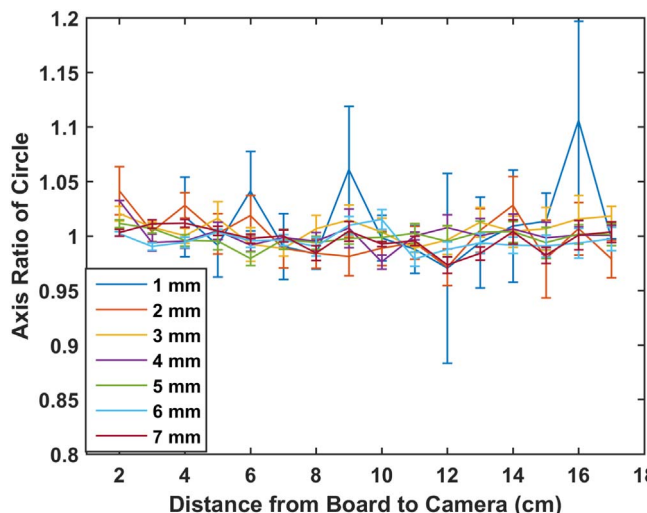


Fig. 5. Mean and standard deviation of the axis ratio versus distance. For a circle, the axis ratio should be 1. The results show that the estimated axis ratios from the pictures are very close to 1 and are not affected by the distance.

overestimated, whereas an underestimate will occur when it is far away from the camera. With two vertical dashed lines in Fig. 6 being at 9 cm and 11 cm and two horizontal dashed lines showing the  $\pm 5\%$  errors, we see that all diameters except 1 mm have  $\sim \pm 5\%$  or smaller error when the board is distanced between 9 cm and 11 cm from the ring edge. Since the theoretical DOF of the original three cameras for the CSU MASC is about 13 mm, we extend the DOF to 26 mm for PSD computation. The applicable DOF needs to be adjusted based on the particle size. Accurate size estimation for a particle falling completely inside the DOF is not problematic; namely, when a particle whose maximum cross section (parallel to the photographic plane) falls inside the DOF, we will have a clear image and estimate size correctly. From this viewpoint, the applicable DOF equals the theoretical DOF plus the size of the particle along the line from the particle center to the center of the lens. Since it is impossible to compute this size, we assume that it is approximately equal to the maximum particle dimension showing on pictures on average. As we can see in Figs. 5 and 6, the 1-mm (white circle diameter) data (blue lines) show higher error than the data for other diameters, which is because a small image on a picture will mess

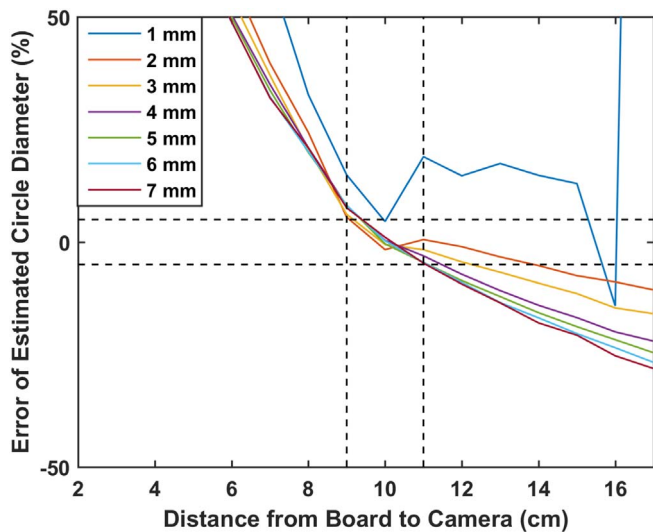


Fig. 6. Relative error of the mean estimated circle diameter, defined in Eq. (7), versus distance. Two vertical dashed lines mark 9-cm and 11-cm distances. Two horizontal dashed lines denote 5% and -5% error levels. From this figure, the applicable DOF is around 2 cm.

up easily with the background of the picture and be easily affected by the random noise on the CCD. These factors will affect the accuracy of image processing. At the same time, for a digital camera picture, a smaller image has a higher digitalization error.

### 3.3. Image processing procedure

To compute the size of a particle from a picture (photograph), we need to detect the particle in the picture first. The first step is to separate the particle image from the picture background. If the camera is fixed and its focus distance is not being changed, such as in the MASC, and pictures are taken in relatively short time intervals, the images of background objects will appear at almost the same position and with

almost the same intensity in these pictures. On the other hand, the images of precipitation objects will appear in the pictures randomly positioned and with different intensities. Since a digital camera stores the picture in a digital format (256 grayscale JPEG for the MASC), each grayscale picture actually is a two-dimensional integer matrix. Each element in this matrix presents the intensity on the corresponding pixel. It is straightforward to compute the mean and the standard deviation of these matrices. The mean represents the background of the picture and the standard deviation accounts for the background and ambient conditions (i.e., temperature and brightness) change during the time, intensity measurement fluctuation, noise on the CCD, and so on. Because the MASC stores pictures taken within an hour into one file folder, we use one hour as the time interval for background computation. The picture to be used to identify precipitation particles and further process their characteristics is obtained from the original (raw) picture by subtracting the mean plus twice the standard deviation. The upper-left panel of Fig. 7 shows a picture taken by the third original MASC camera. Note that two bright dots on the left are the IR emitters. The upper-right panel is the same picture but converted to the  $64 \times 64 \times 64$  RGB format according to the intensity so that more detail of the background can be observed. The bottom-left panel represents the mean picture in the RGB format, and to its right is the picture with the background removed.

After obtaining a picture with background removed, we use a similar procedure as for the SVI (Fig. 4 of Newman et al., 2009) to detect particles in the picture, which is commonly used procedure for image detection. In short, we use the “Sobel method” (Sobel, 1970) to detect the edge of the particle image, dilate the detected edge lines based on the pre-set minimum detectable dimension (0.01 mm in our procedure), fill unwanted holes, and erode the image to get wanted internal holes also based on the minimum dimension (Russ, 2006). Fig. 8 shows an example of this image processing procedure. Note that all sub-figures shown are in the binary black-white (BW) format. The size of the particle can be obtained by counting how many pixels with value 1 are in the particle image. If a particle image has  $M$  such pixels, its cross-sectional area in the picture is:

$$A = M * P_h * P_v \tag{8}$$

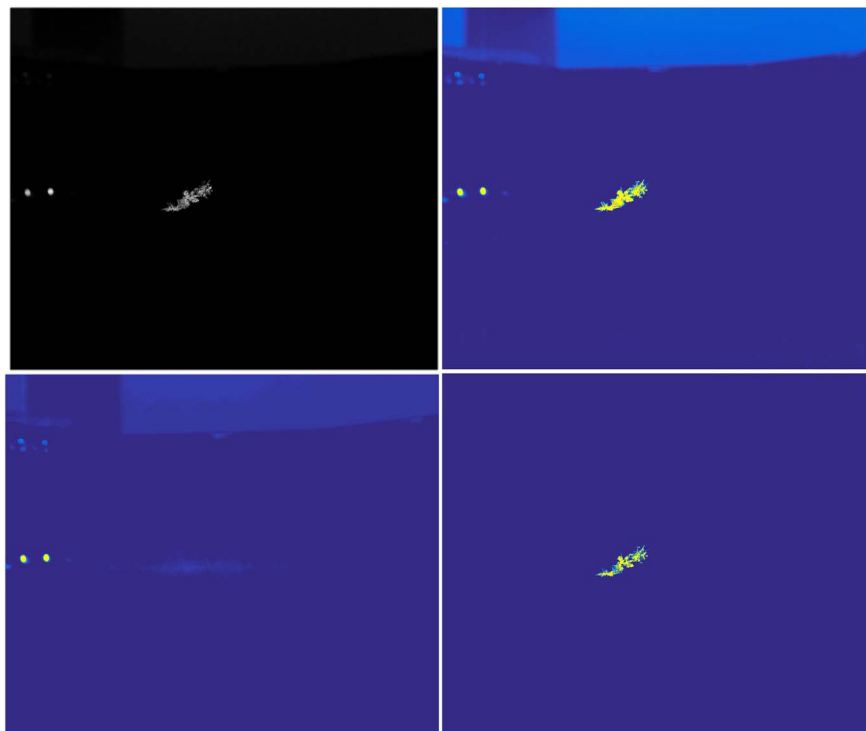


Fig. 7. Example demonstrating the picture background removal procedure. (upper-left panel) Picture taken by the third original MASC camera. (upper-right panel) Exact same as the upper-left panel but displayed in color (RGB). (bottom-left panel) Background of the picture displayed in color. (bottom-right panel) Picture with background removed, displayed in color. (For interpretation of the references to color in this figure legend, the reader is referred to the web version of this article.)

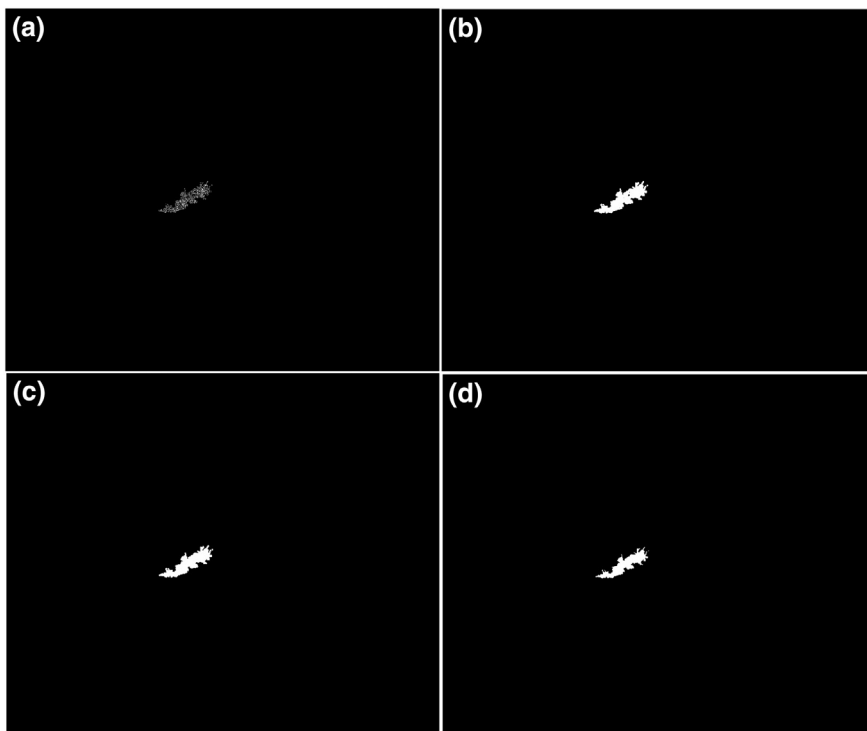


Fig. 8. Example of image processing. (a) Detecting the edge of the particle image in a picture with background removed (picture in the bottom-right panel of Fig. 7). (b) Dilatation of the detected edge lines. (c) Filling the unwanted holes in the image from (b). (d) Eroding the image from (c).

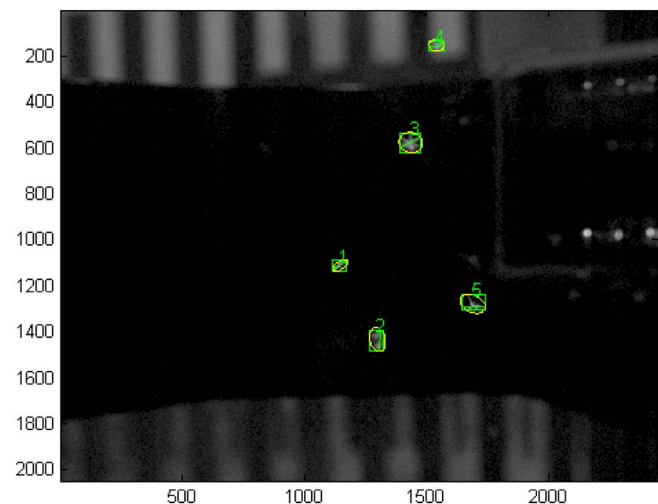


Fig. 9. Example of a multi-flake picture taken by the CSU MASC on 3 March 2015 from 18:00 to 19:00 (UTC). The equi-area circle diameters ( $D_e$ ) of the five particles are 0.96 mm, 1.88 mm, 2.06 mm, 1.06 mm, and 1.31 mm, respectively.

For the axis-symmetric precipitation particles such as rain drops, it is easy to compute the particle volume even from a 2D image. Most researchers use equi-volume spherical diameter to represent the size of a raindrop. However, the winter precipitation particles usually have irregular 3D-shapes, and thus it is impossible to compute their volume from one view (2D picture). Some researchers use maximum dimension to represent the particle size because a freefall particle tends to fall in its maximum dimension. The maximum dimension is measured from point to point of the particle contour. In this paper, we use the equi-area circle diameter,  $D_e$ , defined as the diameter of a circle whose area is equal to the particle cross-sectional area in the picture, to represent the particle size.  $D_e$  is much easier to compute from a picture and it directly relates to the particle volume.

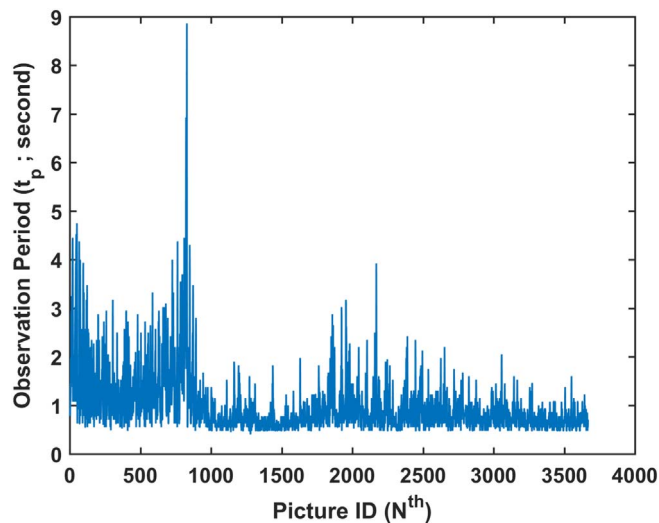


Fig. 10. Example of the observation time period ( $t_p$ ). The total observation time is one hour. During this hour, 3670 pictures were taken by each MASC camera.

#### 4. PSD computation based on MASC experiments

After detecting all particles in a picture (photograph) and computing their geometrical features, we first take out the edge particles. Next, we note that, from the DOF experiment, the intensity of the particle image reduces very fast when it deviates from the focus plane (see Fig. 4). If the maximum intensity of a particle image is lower than 50, the particle is out of the DOF range, and we take out those blurred particle images. In addition, if the total pixel count of a particle image is smaller than 10, this particle is too small to be detected, and the last step is to remove those particle images. Usually those very small images are caused by the remainder of the background or by being too far from the focus plane.

The main features of blurred images were discussed in Section 3.2. To each picture, we apply a range filter given by:

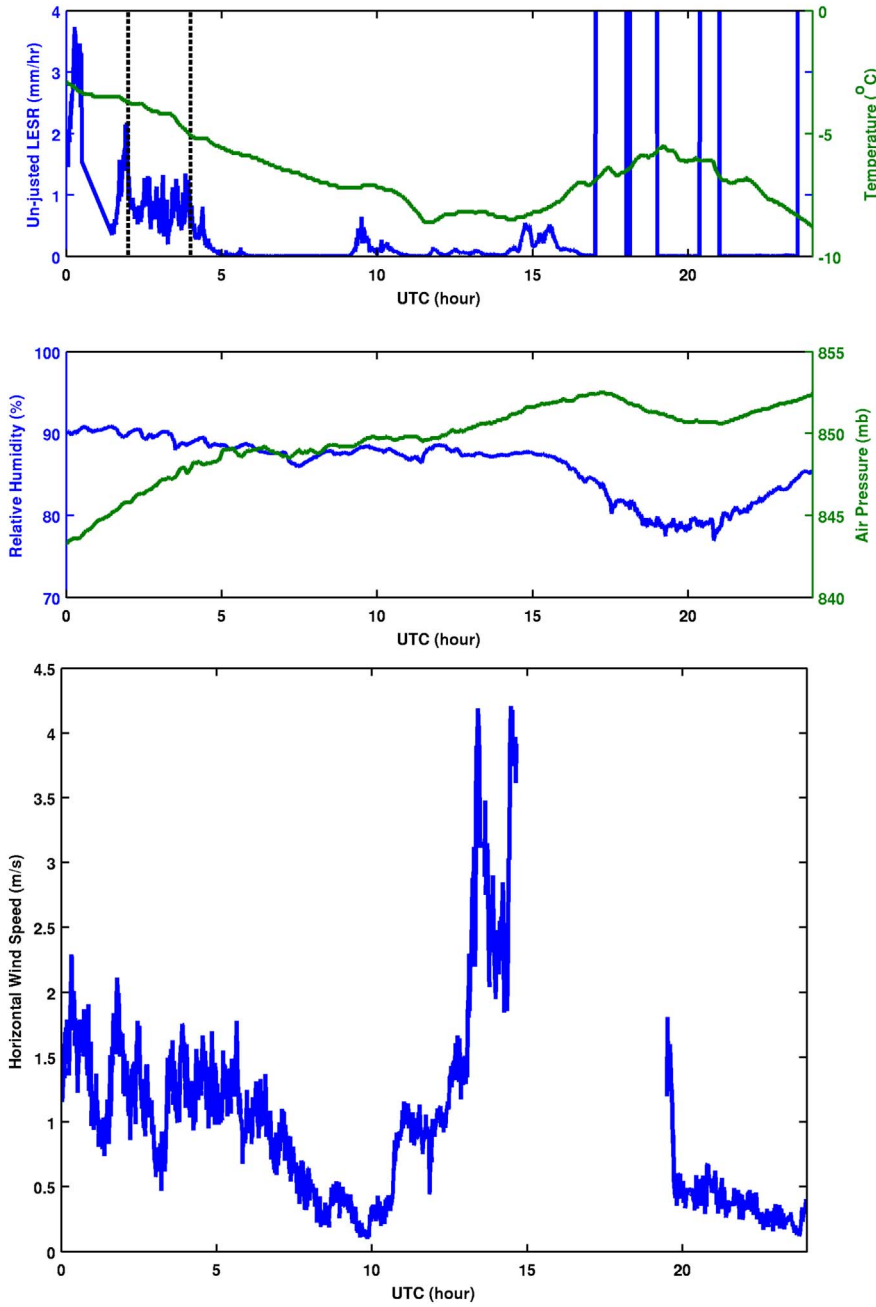


Fig. 11. Environmental conditions of the MASCRAD test site on 26 December 2014. Two vertical black dashed lines in the top panel represent the time period of 02:00 to 04:00 UTC. During this time period, the horizontal wind speed (bottom panel) was around  $1.5 \text{ m s}^{-1}$ .

$$\mathbf{IMr}(ij) = \max[\mathbf{IM}(i - 1: i + 1j - 1: j + 1)] - \min[\mathbf{IM}(i - 1: i + 1j - 1: j + 1)] \quad (9)$$

where  $\mathbf{IM}$  relates to the original picture and  $\mathbf{IMr}$  to the filtered picture. A blurred particle image will have low normalized averaged intensity (normalized by maximum intensity; 255) of both original and filtered images. If the product of the two normalized averaged intensities is smaller than 0.01, we classify the particle image as blurred (Garrett et al., 2012). Fig. 9 shows an example of a multi-flake picture, in which five clear particles were found by our image processing code. The green rectangles are the minimum rectangles including each of the snowflakes, the yellow ellipses are the minimum circumscribed ellipses for each snowflake, and the corresponding equi-area circle diameters are  $D_e = 0.96 \text{ mm}$ ,  $1.88 \text{ mm}$ ,  $2.06 \text{ mm}$ ,  $1.06 \text{ mm}$ , and  $1.31 \text{ mm}$ , respectively.

Once the sizes of all particles are obtained from pictures and are sorted into size bins, we can compute the PSD based on Eq. (2). The size

bin width is not necessarily uniform across the particle sizes. Some disdrometers, such as Joss (Joss and Waldvogel, 1967) or Parsivel (Löffler-Mang, 1998), use large bin widths for big particles because, naturally, the numbers of big particles are much smaller than those of small ones, and the large bin widths can reduce the sampling error for big particles. However, in order to perform comparisons with a 2DVD, for this research we set the bin width as for the 2DVD, so we use a uniform bin width of  $0.25 \text{ mm}$ , with the center values of size bins being from  $0.125 \text{ mm}$  to  $25.125 \text{ mm}$  and the total number of size bins amounting to 101.

With the size of every particle which clearly shows in each picture measured, the particles being sorted into size bins, and the numbers of particles in each size bin being counted, these numbers need to be properly normalized by the measurement volume. In Eq. (2),  $\Delta_t \times V_t$  actually represents the total accumulated volume during the observation time period. From this viewpoint, Eq. (2) is exactly the same as Eq. (4) in Newman et al. (2009). Assuming a very heavy winter storm with

**Table 1**

Overall PSD results for the entire analyzed time period, 02:00Z to 04:00Z, of the 26 December 2014 case. Second column provides the total number of particles for each camera. Third column gives the MASC mean NSD results for each 15-minute observation period specified in the first column of the table. Fourth column presents MASC mean NSDs of all 15-minute intervals obtained using the 2DVD  $D_{app}$ - $D_e$  relationship from Fig. 13. Fifth column shows the 15-minute mean NEs for the MASC-2DVD PSD comparison.

Time (UTC)	# of particles for camera 2, 3, and 4	$\overline{NSD}$ using $D_e$ (%)	$\overline{NSD}$ using $D_{app}$ (%)	$\overline{NE}$ (%)
02:00–02:15	824, 634, and 692	28.9	36.1	78.2
02:15–02:30	1049, 881, and 991	25.2*	27.1	130.0
02:30–02:45	1084, 876, and 1159	28.9	30.7	194.1 <sup>†</sup>
02:45–03:00	953, 613, and 700	45.6	40.1	120.0
03:00–03:15	479, 254, and 268	52.6	43.2	62.3
03:15–03:30	739, 273, and 447	58.2 <sup>†</sup>	60.9	40.3
03:30–03:45	790, 337, and 479	42.6	41.2	8.8*
03:45–04:00	807, 406, and 498	35.8	36.6	23.0
Average		39.73	39.49	82.09

Remarks: \*Best agreement. <sup>†</sup>Worst agreement.

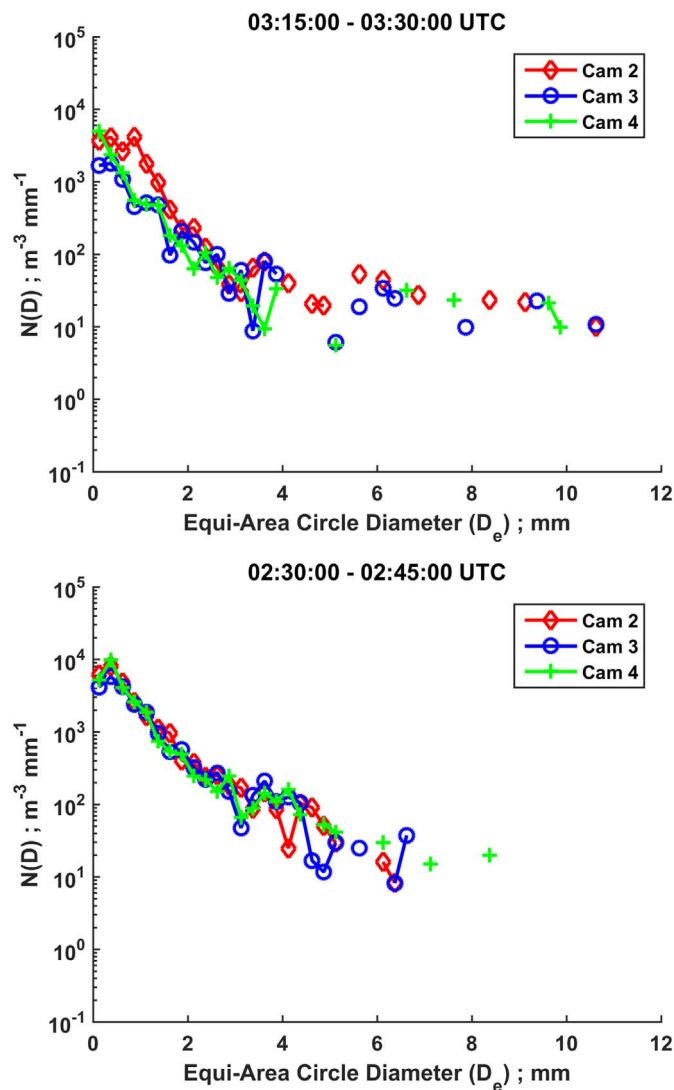


**Fig. 12.** Two examples of MASC single-camera PSD computation for the 26 December 2014 case. (upper panel) Three original MASC single-camera PSDs with the highest mean NSD. (bottom panel) Three PSDs with the lowest mean NSD. Even in the worst case, camera 3 still agrees very well with camera 4.

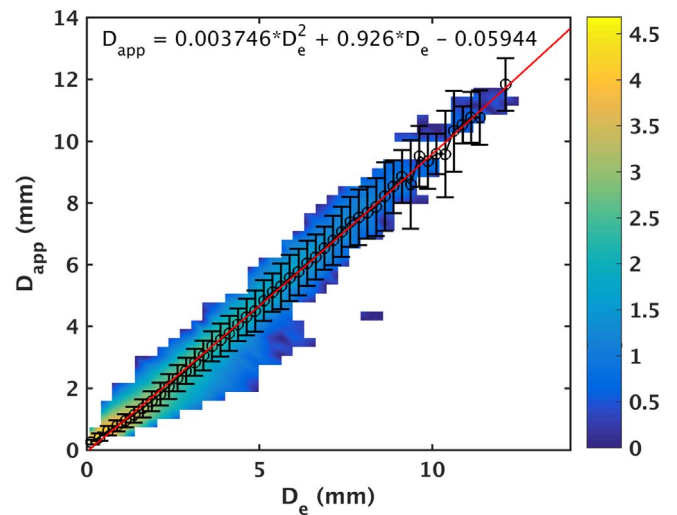


**Fig. 13.**  $D_{app}$  versus  $D_e$  relationship obtained from the collocated 2DVD during the time period 0200Z-0400Z on 26 December 2014. The color contour shows the concentration of particles in log-scale. The black circle-line represents the mean  $\pm 1\sigma$  and the red line is the 3rd order polynomial fit. (For interpretation of the references to color in this figure legend, the reader is referred to the web version of this article.)

the MASC triggering continually, the frame rate would be  $2 \times V_{measurement}$  (in Eq. (6)) is one-second accumulated measurement volume. Every MASC picture is taken when the MASC is triggered by a particle. If  $(N - 1)^{th}$ ,  $N^{th}$ , and  $(N + 1)^{th}$  pictures are taken at time instants  $t_0$ ,  $t_1$ , and  $t_2$ , respectively, the observation period of the  $N^{th}$  picture is from  $(t_1 + t_0)/2$  to  $(t_2 + t_1)/2$ , i.e., it is  $t_p = (t_2 - t_0)/2$  long, and the accumulated volume in this period equals  $t_p \times 2 \times V_{measurement}$ . Fig. 10 shows an example of  $t_p$  for the total observation time of one hour, during which time 3670 pictures were taken by each MASC camera. The longest  $t_p$  is 8.8630 s and the shortest is 0.4035 s.

The sampling error of the PSD directly relates to the accumulated measurement volume (numerically it is approximately equal to the observation volume but smaller). Using Eqs. (5) and (6) of Newman et al. (2009), the measurement volume of the SVI for a 5-mm particle amounts to  $60 \times 0.117 \times 5 \times 10^{-6} \times (32-5) \times (24-5) \text{ m}^3 \text{ s}^{-1} \approx 0.018 \text{ m}^3 \text{ s}^{-1}$ . The observation area of the 2DVD is around  $0.01 \text{ m}^2$ . Using Eq. (6) of Huang et al. (2015), the observation volume of a particle falling at the speed of  $1 \text{ m s}^{-1}$  is  $0.01 \text{ m}^3 \text{ s}^{-1}$ . Considering one MASC camera with 12.5-mm lens, 2/3" CCD, and 100-mm focus distance, such as the cameras of the CSU MASC, the FOV is 70.4 mm by 52.8 mm and DOF is 20 mm. The maximum observation volume from Eq. (4) is about  $0.00015 \text{ m}^3 \text{ s}^{-1}$ . Comparing one-second observation volume of the MASC with the SVI and the 2DVD, it is obvious that the MASC is not well suited for one-minute averaged PSD, as is usually done with both the SVI and the 2DVD. We need to extend the observation period to compensate for the spatial insufficiency of observations. Note that the SVI usually involves blurred particle images to extend its DOF, which increases uncertainty. If we only compare the FOV and frame rate of the MASC with the SVI, the ballpark estimation of observation time is at least 6 minutes. So, in this paper, we compute 15-minute averaged PSD of the MASC.

### 5. PSD MASC measurements, results, and discussion

Next, we present PSD MASC measurements and results for two characteristic snow events to demonstrate the performance of the novel PSD algorithm. Two selected cases from the MASCRAD campaign (Notaroš et al., 2016) are the 26 December 2014 and 21 February 2015 snow observation/analysis events. In addition to comparing the results for individual MASC cameras, we compare MASC mean PSD (averaged over three cameras) with the collocated 2DVD (see the upper-right

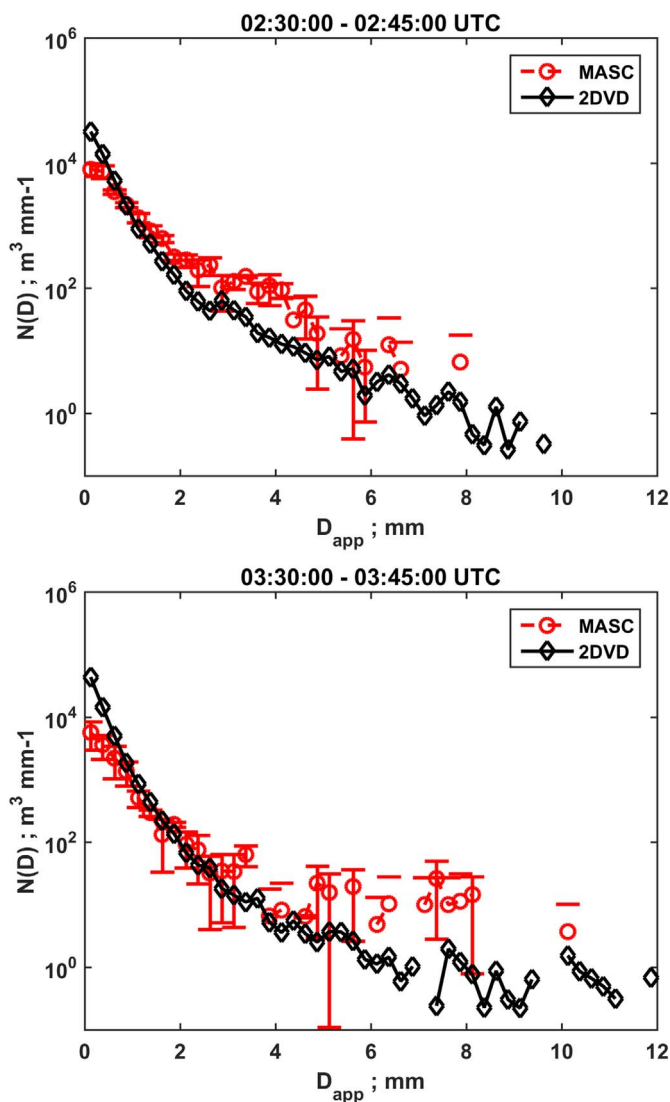


Fig. 14. Comparison of the MASC mean PSD with the 2DVD PSD for the 26 December 2014 case. (upper panel) Period 0230Z–0245Z with the worst agreement between the 2DVD and the MASC. The mean NE for this period is 194.1%. (bottom panel) Period 0330Z–0345Z with the best agreement. The mean NE is 8.8%.

panel of Fig. 1.).

### 5.1. Case 1: 26 December 2014 snow event

Fig. 11 shows the environmental conditions of the MASCRAD test site (Notaroš et al., 2016) on 26 December 2014. The blue line of the top panel is unadjusted liquid-equivalent snow rate (SR) which is based on the PSD of a collocated 2DVD and assumes the Ikeda-Brandes (Brandes et al., 2007) density-size relationship. Although the SR is only an estimate, the tendency is still maintained. Two vertical black dashed lines in the top panel represent the time period of 02:00Z to 04:00Z, which was the period with the highest snow rate and with the 2DVD working normally. During this period, the horizontal wind speed was around  $1.5 \text{ m s}^{-1}$ , so calm wind conditions. In each 15-minute time interval, we compute the averaged (over 15 min) PSD for each camera. Since the three MASC cameras look at approximately the same point, the PSDs from the three cameras should be very similar. To quantify the measurement fluctuations, we compute the mean NSD for each 15-minute averaged PSD on each size bin. There are two quantities directly related to the PSD in radar meteorology, namely, the SR and the radar reflectivity factor (Z). Locatelli and Hobbs (1974) show that the

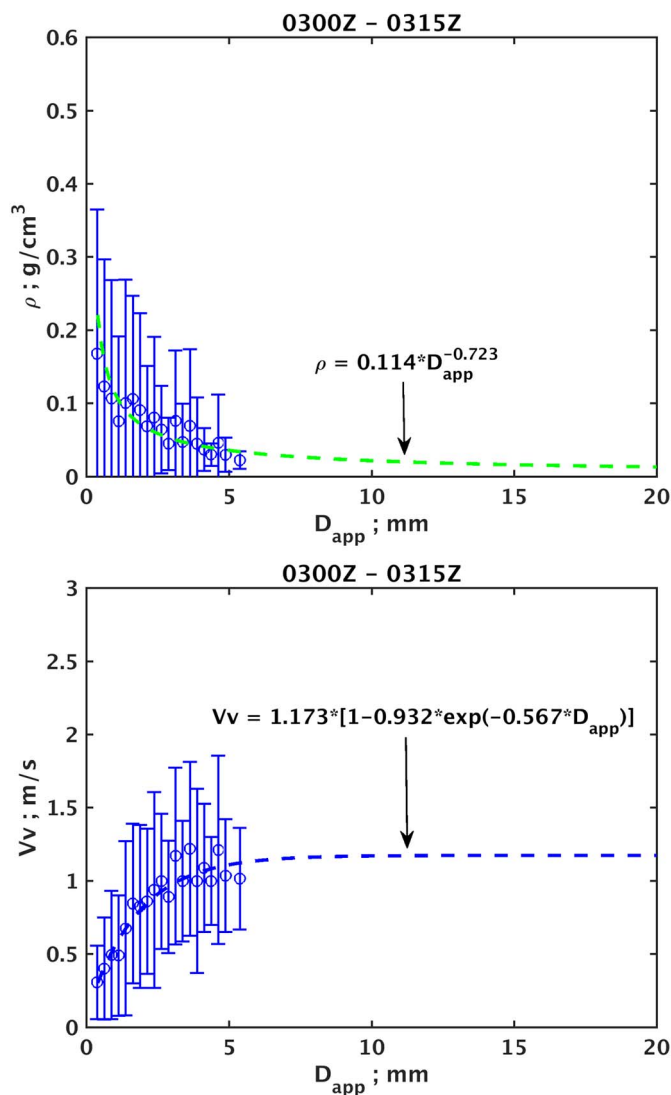


Fig. 15. Example of density-size (upper panel) and fall speed-size (bottom panel) relations at 0300Z–0315Z on 26 December 2014. These relationships are based on the 2DVD single-camera data.

exponent of mass-size power-law relationship for an aggregated and unrimed snowflake is 1.9, and Table 1 of Mitchell et al. (1990) shows that the exponents for different types of ice precipitation are around 2 except for short columns and hexagonal plates. Therefore, the exponent of density-size power-law relationship is approximately  $-1$ . If we consider this density-size relationship, the SR is roughly proportional to the 2nd moment of the PSD and, in Rayleigh region, the Z is proportional to the 4th moment of the PSD for ice precipitation. The mean NSD is, then, weighted by the 3rd moment of the mean PSD, and is computed as:

$$\text{NSD} = \sum_{i=1}^{101} \text{NSD}(D_i) \cdot \text{WT}(D_i) \quad (10)$$

where  $\text{NSD}(D_i)$  is the normalized standard deviation of the  $i^{\text{th}}$  size bin. WT is a weight function defined as:

$$\text{WT}(D_i) = \frac{D_i^3 \cdot \text{ND}_{\text{MASC}}(D_i)}{\sum_{i=1}^{101} D_i^3 \cdot \text{ND}_{\text{MASC}}(D_i)} \quad (11)$$

where  $\text{ND}_{\text{MASC}}$  is the mean PSD of three cameras, which, when used to compute the weight function, only accounts for bins whose concentration is nonzero for all cameras, to avoid a very high standard deviation due to a no-sample situation in a size bin.

Fig. 12 shows two examples of MASC single-camera PSD

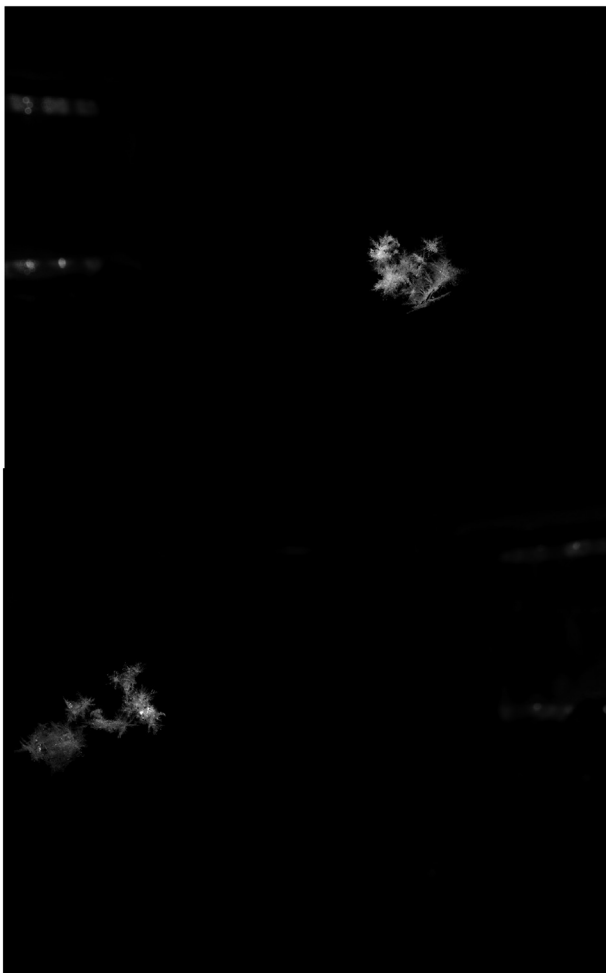


Fig. 16. Images of two large particles taken by the MASC at 0300Z–0315Z on 26 December 2014. The corresponding  $D_e$ s are 9.04 mm (upper panel) and 9.54 mm (bottom panel). The highly lit spots on the particles are the rime.

computation. The camera IDs of the three original MASC cameras are 2, 3, and 4, counted clockwise. The upper panel shows the results for the 15-minute observation period from 0315Z to 0330Z, for which the three PSDs have the worst agreement, with a 58.2% mean NSD. Even for this worst case, the PSDs of cameras 3 and 4 are still in an excellent agreement. The bottom panel of Fig. 12 shows the best agreement, from 0215Z–0230Z, with a 25.2% mean NSD. Table 1 shows the overall PSD results for the entire analyzed time period, 02:00Z to 04:00Z. The mean NSD over this 2-hour time is 39.2% and the results for each 15-minute observation period are shown in the second column of the table. To cross-validate  $ND_{MASC}$ , we have also computed the PSD of the collocated 2DVD ( $ND_{2DVD}$ ) and compared the two sets of results. The 2DVD uses apparent diameter ( $D_{app}$ ) for its PSD (Schönhuber et al., 2000; Huang et al., 2015). It computes the particle volume from two views by assuming symmetry between two views for each scan line. Because the shape of an ice particle is irregular, this volume cannot be claimed as the true volume, and is thus called the apparent volume, with  $D_{app}$  denoting its equi-volume spherical diameter. At the same time, the 2DVD can also compute  $D_e$  based on one view. Since the MASC and the 2DVD were collocated, this 2DVD  $D_{app}$ - $D_e$  relationship can also apply to the MASC. Fig. 13 shows the  $D_{app}$  versus  $D_e$  relationship obtained from the 2DVD during the same time period. The color contour represents the concentration of particles in log-scale and the red line is the 3rd order polynomial fit. We have applied this relationship to convert every particle found by our PSD procedure from  $D_e$  to  $D_{app}$ , have recomputed the PSD for each camera, and recalculated the  $ND_{MASC}$  and standard

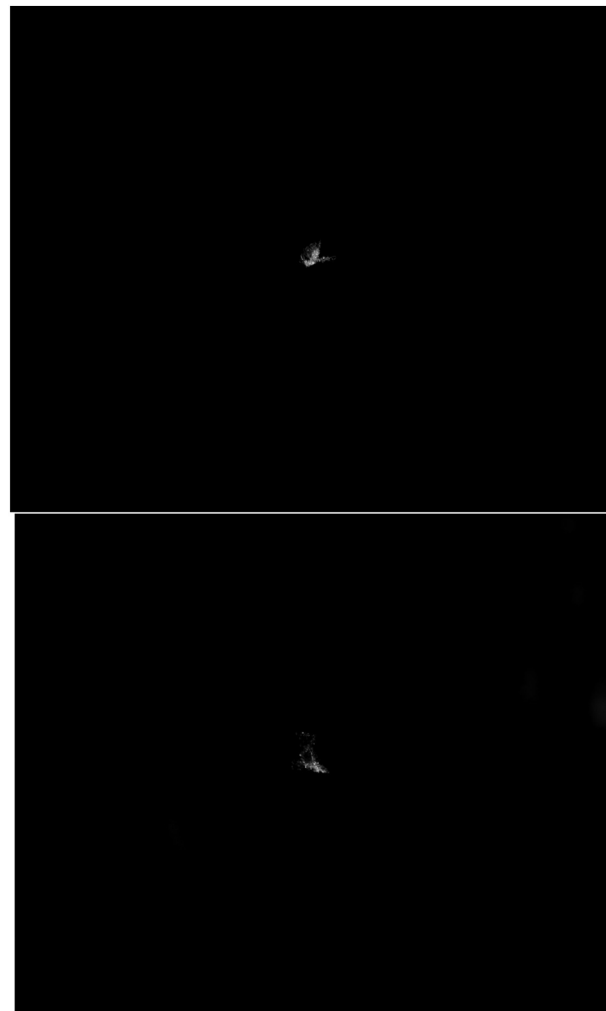


Fig. 17. MASC images of two small particles at 0300Z–0315Z on 26 December 2014, with the corresponding  $D_e$ s amounting to 1.35 mm (upper panel) and 1.40 mm (bottom panel). The pictures have been enlarged twofold (by cropping) to enhance the clarity of the small particle images.

deviation for each size bin. The mean NSDs of all 15-minute intervals are given in the third and fourth columns of Table 1. Note that converting  $D_e$  to  $D_{app}$  is only for comparing with the 2DVD (comparing the MASC PSD with the 2DVD PSD), which uses  $D_{app}$  as size parameter. When we employ the MASC only, we can use  $D_e$ , or more commonly,  $D_{max}$  (maximum dimension) for size characterization.

To compare  $ND_{2DVD}(D_{app})$  with  $ND_{MASC}(D_{app})$ , we have assumed that  $ND_{2DVD}$  is “true” PSD, have calculated the normalized error (NE) for each size bin, and computed weighted mean NE for the whole PSD using the same method as in Eqs. (10) and (11) except for replacing NSD by NE and  $ND_{MASC}$  by  $ND_{2DVD}$ . Fig. 14 shows two examples of the MASC-2DVD PSD comparison. The red line is the MASC mean PSD with  $\pm 1\sigma$  and the black line is the 2DVD PSD, which is computed using Huang et al., 2015 method. The upper panel in Fig. 14 shows the worst agreement between the 2DVD and the MASC, with 194.1% mean normalized error at 0230Z–0245Z, whereas the bottom panel shows the best agreement, with 8.8% mean normalized error. The overall normalized error for this case is 82.1% and the 15-minute mean NEs is given in the fifth column of Table 1. Note that MASC can produce usable standalone PSD results, that is, we can compute the PSD based on the MASC only, and it does not need a 2DVD. In our study, the collocated 2DVD is used to validate the MASC PSD. Namely, the MASC instrument is relatively new and the proposed new technique for MASC PSD measurement and computation is validated by comparison with a

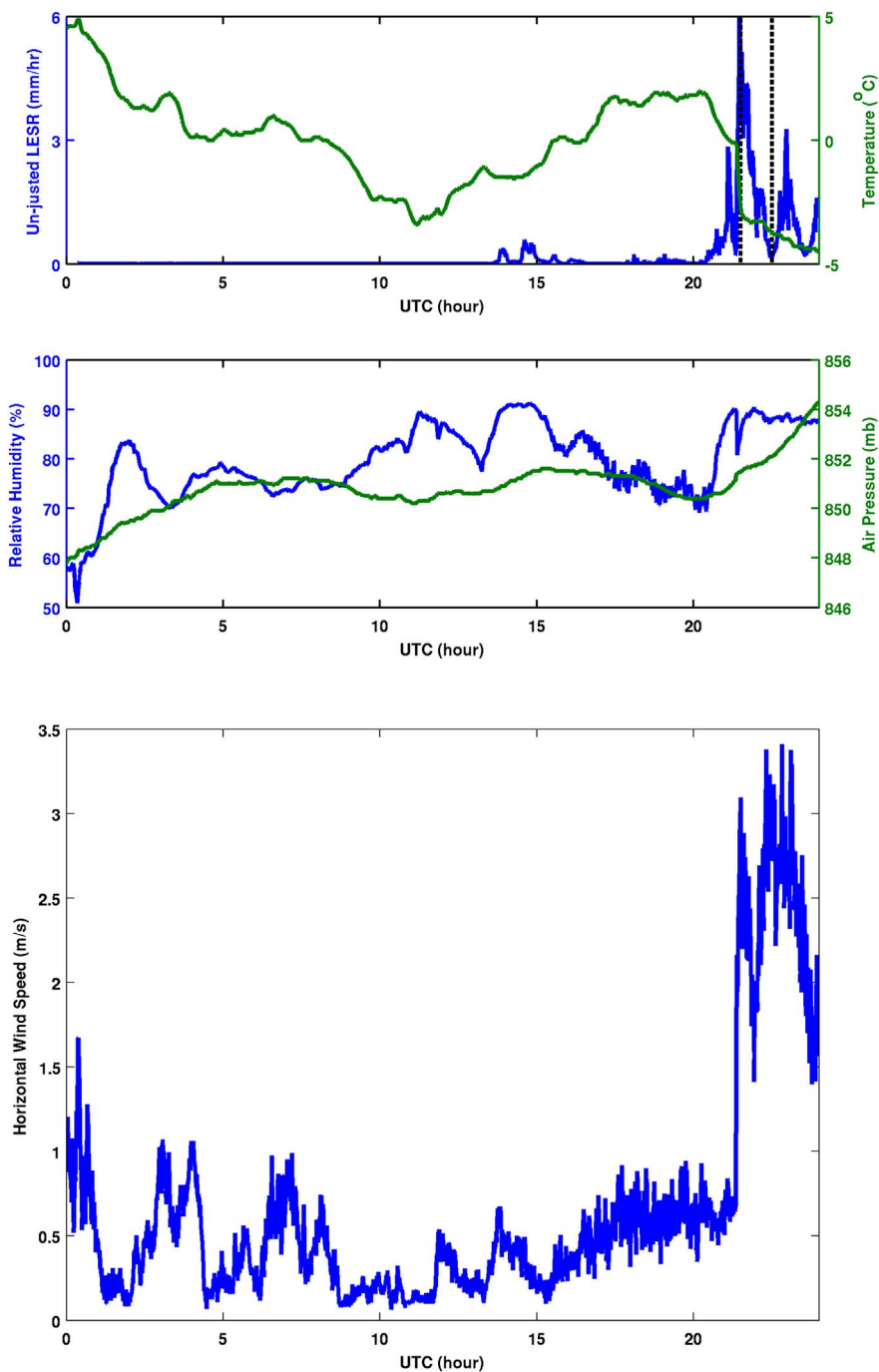


Fig. 18. Same as in Fig. 11 but for the 21 February 2015 MAS-CRAD case. Two black dashed vertical lines in the top panel denote the analyzed time period, from 2130Z to 2230Z.

more established instrument such as the 2DVD.

Based on Fig. 13, this case has the intercept parameter smaller than  $10^5$  (see the color bar) and particle sizes up to 12 mm. The large sized winter precipitation particles usually are aggregate snowflakes. The density-size power-law relationship from the 2DVD analysis (Huang et al., 2015) shows that the respective coefficient is from 0.178 to 0.113 and the exponent is from  $-0.774$  to  $-0.723$  during the time 0245Z to 0315Z. Fig. 15 shows an example of density-size (top panel) and fall speed-size (bottom panel) relationships at 0300Z to 0315Z. Note that for size bins with fewer than 10 particles, the mean and standard deviation are not considered meaningful and are therefore not shown. Brandes et al. (2007) showed that a typical Colorado dry aggregate snow event has a power-law relationship with coefficient 0.178 and exponent  $-0.922$ . The light degree of riming will increase the density of large aggregate snowflakes. Therefore, the higher exponent of our

analyzed case implies the occurrence of aggregate snow with some degree of riming. Fig. 16 shows the images of two large particles (9.04 mm and 9.54 mm) taken by the MASC at 0300Z to 0315Z. We can easily identify the aggregation from the structure of snowflakes. The highly lit spots on the snowflakes are the rime. Fig. 17 shows the MASC images of two small particles (1.35 mm and 1.40 mm) from the same time period. Note that the pictures have been enlarged so that these small particles can be seen clearly. All four particles are in the DOF because they passed the blur examination. However, the intensities of particle images are not very high, which is most likely due to fluffy structure of aggregate snow. Most of light passes through and does not reflect back to the cameras. This conclusion can also be confirmed by the low fall speed ( $\sim 1 \text{ m s}^{-1}$ ) of large particles in the bottom panel of Fig. 15.

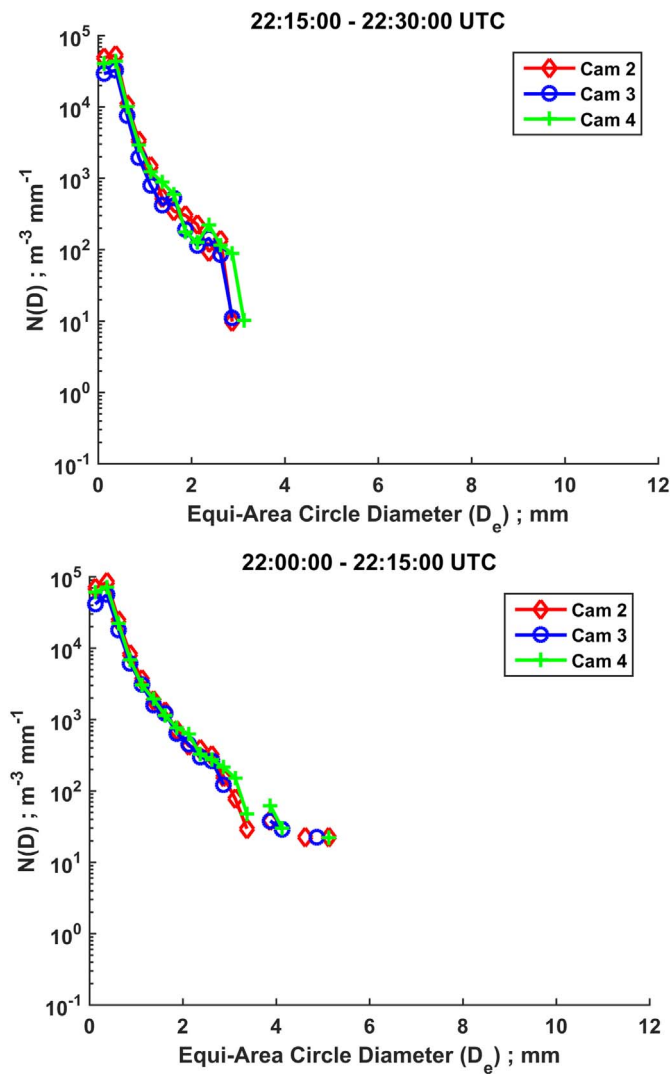


Fig. 19. Same as in Fig. 12 but for the 21 February 2015 event. (top panel) Period 2215Z–2230Z with the worst agreement between the three MASC individual cameras' PSDs and 33.1% mean NSD. (bottom panel) Period 2200Z–2215Z with the best agreement and 14.6% mean NSD.

Table 2

Same as in Table 1 but for the 21 February 2015 case.

Time (UTC)	# of particles for camera 2, 3, and 4	$\overline{NSD}$ using $D_e$ (%)	$\overline{NSD}$ using $D_{app}$ (%)	$\overline{NE}$ (%)
21:30–21:45	8354, 5613, and 7181	22.0	18.3	14.3*
21:45–22:00	6371, 4246, and 5660	22.5	21.9	31.6
22:00–22:15	6066, 4031, and 5727	14.6*	14.6	77.3
22:15–22:30	4288, 2745, and 4020	33.1 <sup>†</sup>	23.7	189.0 <sup>†</sup>
Average		23.05	19.63	78.05

Remark: \*Best agreement. <sup>†</sup>Worst agreement.

### 5.2. Case 2: 21 February 2015 snow event

The second case we analyze was on 21 February 2015, and Fig. 18 shows the environmental conditions on this day. The main snow storm started around 2000Z and continued to the next day. Two black dashed lines are at 2130Z and 2230Z bounding the analyzed time period. During this period, the wind speed was around 2.5 to 3 m s<sup>-1</sup>, which is higher than the previous case. Fig. 19 shows two examples of MASC single-camera PSD comparison. The worst agreement between the three cameras' PSDs is at 2215Z–2230Z, with 33.1% mean NSD, and the best

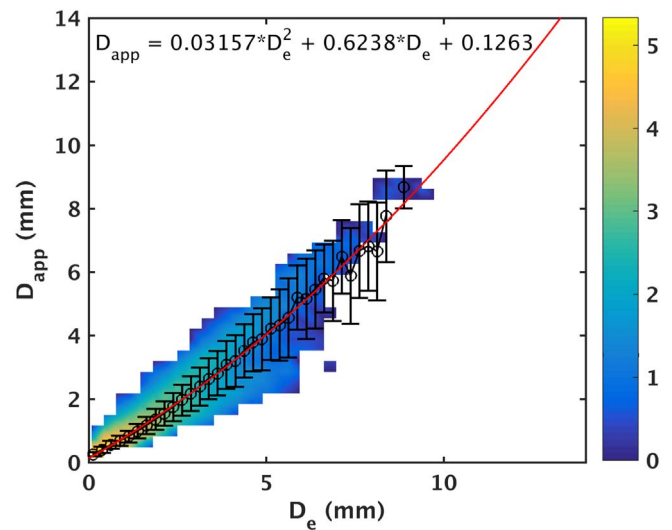


Fig. 20. Same as in Fig. 13 but for the 21 February 2015 case. When compared with Fig. 13, this case has higher intercept parameter ( $> 10^5$ ; see the color bar) than the 26 December case ( $< 10^5$ ) and smaller maximum particle size ( $\sim 9$  mm compared to  $\sim 12$  mm).

agreement is at 2200Z–2215Z, with 14.6% mean NSD.

The mean NSDs for each 15-minute interval are given in Table 2. Although the wind was stronger than for the 26 December 2014 case (2.5 m s<sup>-1</sup> compared to 1.5 m s<sup>-1</sup>), the overall mean NSD was lower (23.05% compared to 39.73%). It appears that the wind speed is not a main factor affecting the self-consistency of the MASC PSD.

Fig. 20 shows the  $D_{app}$  to  $D_e$  relationship from the 2DVD during 2130Z to 2230Z. We have converted  $D_e$  to  $D_{app}$  using the 3rd order polynomial equation given in the figure inset, and have compared  $ND_{MASC}$  with  $ND_{2DVD}$ . Fig. 21 shows two examples of such comparison, with the top panel illustrating the worst MASC-2DVD agreement, with 189% mean NE at 2215Z to 2230Z, and the best agreement, with 14.3% mean NE at 2130Z to 2145Z, being depicted in the bottom panel. The overall mean NE for the entire analyzed one-hour period is 78.05%, and the mean NEs for each 15-minute observation interval are also given in Table 2. Since this is a stronger-wind case compared with the 26 December 2014 case, it comes out that the wind speed also does not considerably affect the agreement between the MASC and 2DVD PSDs.

Based on Fig. 20, this one-hour event has the intercept parameter larger than  $10^5$  and particle sizes up to 8 mm. Compared with the previous case, this event has more particles but the sizes of particles are smaller. Fig. 22 shows the density-size and fall speed-size relationships of this one-hour period. The density-size relationship cannot be fitted into a power-law form, so we fit it by a 5th order polynomial. A more complex relationship usually indicates that there is no dominant type of snow, i.e., there is compact snow mixed with fluffy aggregate snow. Fig. 23 shows two large particles with sizes of 9.13 mm (top panel) and 7.45 mm (bottom panel). Higher intensities of images indicate that the structures of snowflakes are more solid. They are aggregate snowflakes with a higher degree of riming. The higher fall speed ( $\sim 2$  m s<sup>-1</sup>) for large particles in Fig. 22 also confirms this result. Fig. 24 shows two small particles with sizes of 1.81 mm (top panel) and 1.48 mm (bottom panel). As can be observed based on the higher intensities of images, these particles are compact snowflakes. The density-size relationship given in Fig. 22 yields  $\sim 0.28$  g cm<sup>-3</sup> on average for the density of these particle sizes, and also confirms the MASC observations.

## 6. Summary and conclusions

This paper has proposed the methodology for obtaining the winter precipitation particle size distribution measured by the Multi-Angle

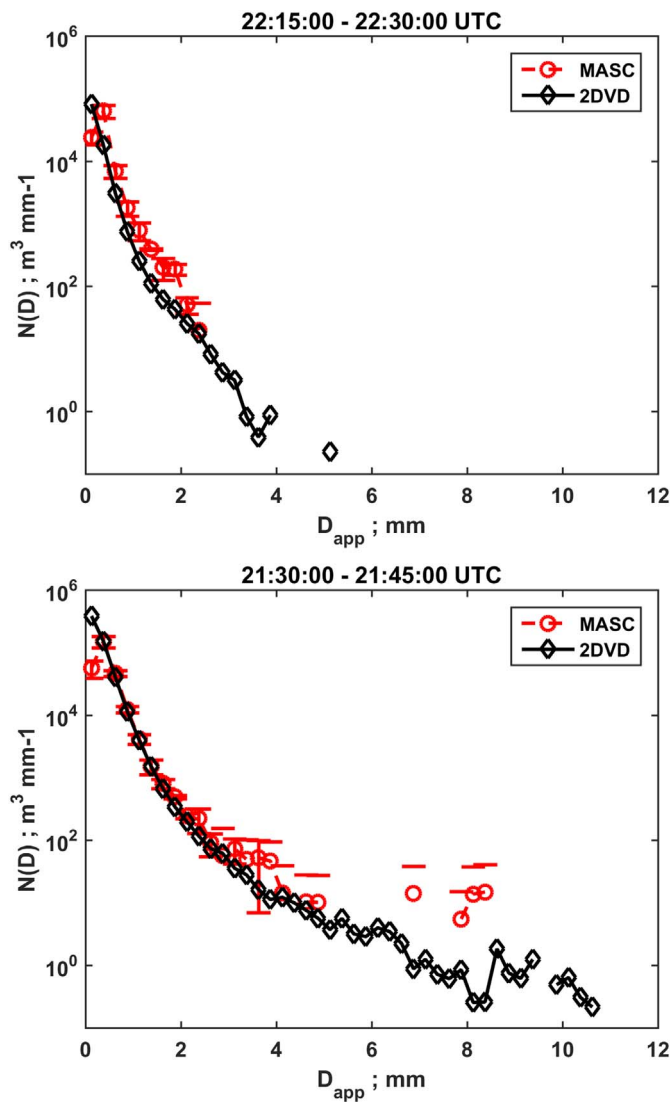


Fig. 21. Same as in Fig.14 but for the 21 February 2015 case. (upper panel) Period 2215Z–2230Z with the worst MASC-2DVD agreement and the mean NE of 189%. (bottom panel) Period 2130Z–2145Z with the best agreement and 14.3% mean NE.

Snowflake Camera, and has presented and discussed the development, implementation, and application of the new technique for PSD computation based on MASC images. MASC is a relatively new ground based instrument for winter event observation, designed to capture high resolution photographs of winter precipitation particles from three different angles. However, the results from the MASC are usually presented as monthly or seasonally, and particle sizes are given as histograms, no previous studies have used the MASC for a single storm study, and no researchers use MASC to measure the PSD. In this paper, we have first provided a brief introduction to the MASC and explained the lens and camera selection criteria. Based on the specification of lenses and cameras and experiments, we have derived the measurement volume of the MASC, and proposed and explained the method and procedure for computing the PSD using MASC images. Since the measurement volume of the MASC is very small compared to the SVI and 2DVD, it is not suitable to measure a short time (one minute) PSD. The longer integration time is necessary to reduce the sampling error. We have also presented an image processing method to measure the size of particles from MASC photographs.

We have derived 15-minute average PSDs for two snow storms of the MASCAD campaign; we have discussed in detail the PSD MASC experiments and results for the 26 December 2014 and 21 February

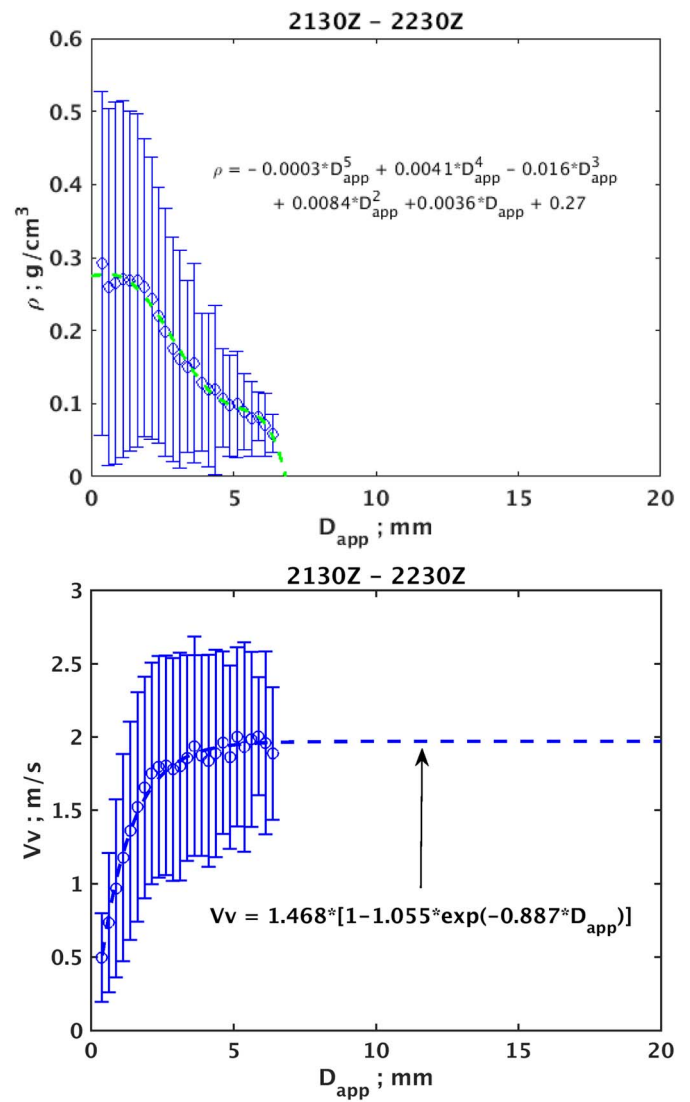


Fig. 22. Same as in Fig. 15 but for the event on 21 February 2015 from 2130Z to 2230Z. The density-size relationship is fitted with a 5th order polynomial. The fall speed-size relationship is fitted with an exponential form.

2015 snow events. The self-consistency of the MASC measured PSD is good. The mean normalized standard deviation for the first case (two hours) is 38.73% and 23.05% for the second case (one hour). The average mean NSD for the two cases is 34.1%. Since the uncertainty due to image processing is the same for three cameras, the averaged mean NSD mainly represents the sampling error of the MASC. To cross-validate PSD measurements, we further compared MASC mean PSD (average over three cameras) with the collocated 2DVD. The maximum NE is 194.1% and the minimum NE is 8.8%. Generally, the MASC PSD is underestimating in the first two size bins of 0.125 mm and 0.375 mm. The concentration of the 2DVD PSD in these two size bins is not very reliable because the horizontal resolution is about 0.16–0.17 mm for the 2DVD. Moreover, a small particle is difficult to match, and hence the 2DVD has significant matching errors for small particles. On the other hand, the MASC has much higher resolution (~0.030 mm). We believe that MASC concentrations in these two size bins are more reliable. From 0.375 mm up to 4.125 mm, MASC concentrations usually agree with the 2DVD very well. The MASC always overestimates for larger size bins, where the concentrations of the 2DVD PSD are very reliable, since the large-size particles are easy to match. A large particle has a large surface area to reflect light especially if highly rimed, and it can thus be miss-classified as a clear image when it actually is blurred.

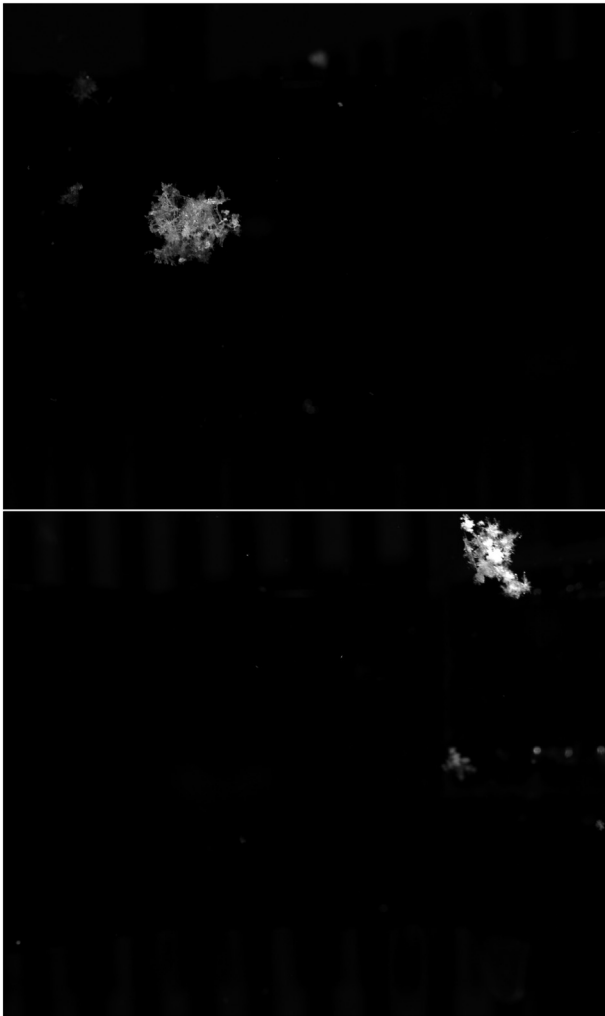


Fig. 23. Same as in Fig. 16 but for 21 February 2015 between 2130Z and 2230Z. The corresponding  $D_{e,s}$  are 9.13 mm (upper panel) and 7.45 mm (bottom panel).

This means that a large particle slightly away from the applicable DOF may still be identified by our image processing technique and included in the PSD computation. Therefore, it is very possible that we are effectively underestimating the measurement volume, mainly underestimating the applicable DOF, for large particles, and so subsequently overestimating the particle concentration.

This is the first study of the MASC PSD. While this paper has proposed and built a framework to compute the PSD of winter precipitation using MASC images, many components of the methodology can still be improved. The image processing procedure can be improved to avoid mixing up small particle images with the background, and the blur examination method can be fine-tuned to avoid miss-classification of blurred images so that we can overcome the overestimation of concentrations at large size bins. Another component of our future work in this area is to redesign the DOF experiment to improve the particle size estimation, which may lead to an increase of the applicable DOF and further reduction of the sampling error. Moreover, a resulting increase of the measurement volume, by potentially increasing the applicable DOF, may, in turn, enable computation of the short time (e.g., one minute) PSD.

#### Acknowledgements

This work was supported by the National Science Foundation under Grant AGS-1344862. We thank Prof. Timothy Garrett of the University

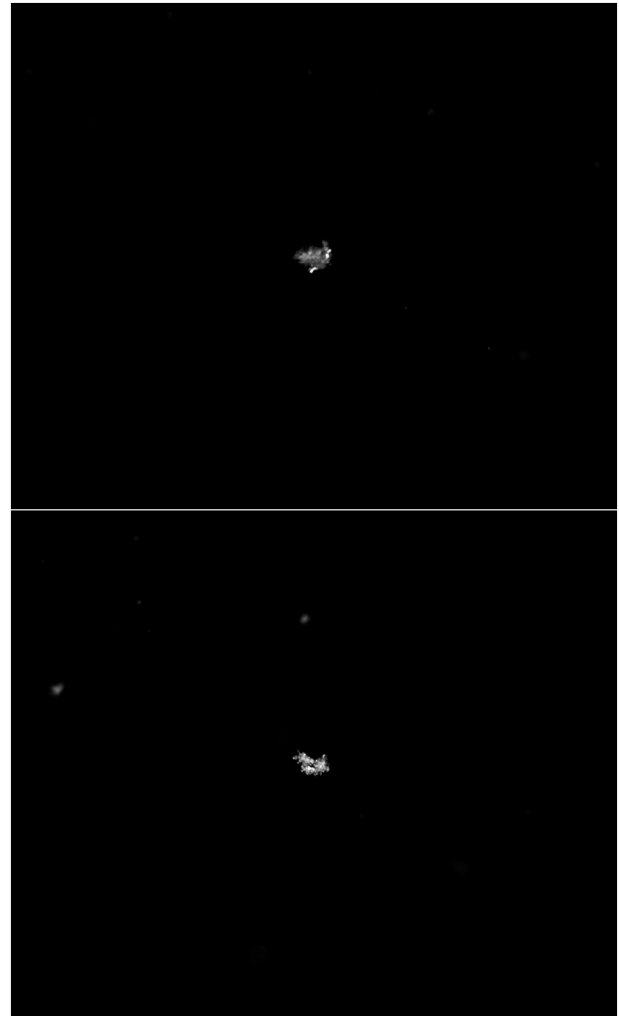


Fig. 24. Same as in Fig. 17 but for the 21 February 2015, 2130Z–2230Z, case, with the corresponding  $D_{e,s}$  of 1.81 mm (upper panel) and 1.48 mm (bottom panel).

of Utah for providing the MASC research code and Mr. Cale Fallgatter of Fallgatter Technologies for helping us understand the hardware and firmware of the MASC.

#### References

- Barthazy, E., Göke, S., Schefold, R., Högl, D., 2004. An optical array instrument for shape and fall velocity measurements of hydrometeors. *J. Atmos. Ocean. Technol.* 21, 1400–1416.
- Böhm, H.P., 1989. A general equation for the terminal fall speed of solid hydrometeors. *J. Atmos. Sci.* 46, 2419–2427.
- Böhm, J.P., 1992. A general hydrodynamic theory for mixed-phase microphysics. Part I: drag and fall speed of hydrometeors. *Atmos. Res.* 27, 253–274.
- Brandes, E.A., Ikeda, K., Zhang, G., Schönhuber, M., Rasmussen, R.M., 2007. A statistical and physical description of hydrometeor distributions in Colorado snowstorms using a video disdrometer. *J. Appl. Meteorol. Climatol.* 46, 634–650.
- Fujiyoshi, Y., Endoh, T., Yamada, T., Tsuboki, K., Tachibana, Y., Wakahama, G., 1990. Determination of a Z-R relationship for snowfall using a radar and high sensitivity snow gauges. *J. Appl. Meteorol.* 29, 147–152.
- Garrett, T.J., Fallgatter, C., Shkurko, K., Howlett, D., 2012. Fallspeed measurement and high-resolution multi-angle photography of hydrometeors in freefall. *Atmos. Meas. Tech. Discuss.* 5, 4827–4850.
- Heymsfield, A.J., Westbrook, C.D., 2010. Advances in the estimation of ice particle fall speeds using laboratory and field measurements. *J. Atmos. Sci.* 67, 2469–2482.
- Heymsfield, A.J., Bansemer, A., Schmitt, C., Twohy, C., Poellot, M.R., 2004. Effective ice particle densities derived from aircraft data. *J. Atmos. Sci.* 61, 982–1003.
- Huang, G., Bringi, V.N., Cifelli, R., Hudak, D., Petersen, W.A., 2010. A methodology to derive radar reflectivity–liquid equivalent snow rate relations using C-band radar and a 2D video disdrometer. *J. Atmos. Ocean. Technol.* 27, 637–651.
- Huang, G., Bringi, V.N., Moisseev, D., Petersen, W.A., Bliven, L., Hudak, D., 2015. Use of 2D-video disdrometer to derive mean density–size and  $Z_e$ –SR relations: four snow

- cases from the light precipitation validation experiment. *Atmos. Res.*, vol. 153, 34–48.
- Joss, J., Waldvogel, A., 1967. A raindrop spectrograph with automatic analysis. *Pure Appl. Geophys.*, vol. 68, 240–246.
- Kleinkort, C., Huang, G.-J., Bringi, V.N., Notaroš, B.M., 2016. Visual hull method for realistic 3D particle shape reconstruction based on high-resolution photographs of snowflakes in freefall from multiple views. *J. Atmos. Ocean. Technol.*. <http://dx.doi.org/10.1175/JTECH-D-16-0099.1>. (Early Release).
- Larmore, Lewis, 1965. *Introduction to Photographic Principles*, 2nd ed. Dover Publications, Inc., New York, pp. 161–166.
- Liao, L., Meneghini, R., Tokay, A., Bliven, L., 2016. Retrieval of snow properties for Ku- and Ka-band dual-frequency radar. *J. Appl. Meteorol. Climatol.* 55, 1845–1858.
- Locatelli, J.D., Hobbs, P.V., 1974. Fall speeds and masses of solid precipitation particles. *J. Geophys. Res.* 79, 2185–2197.
- Löffler-Mang, M., 1998. A laser-optical device for measuring cloud and drizzle drop size distributions. *Meteor. Z.* 79, 53–62.
- Magono, C., Lee, C.W., 1966. Meteorological classification of natural snow crystals. *J. Fac. Sci. II*, 321–335 Hokkaidō University, Japan, Ser. VII.
- Matrosov, S.Y., Campbell, C., Kingsmill, D., Sukovich, E., 2009. Assessing snowfall rates from X-band radar reflectivity measurements. *J. Atmos. Ocean. Technol.* 26, 2324–2339.
- Mitchell, D.L., Zhang, R., Pitter, R.L., 1990. Mass-dimensional relationships for ice particles and the influence of riming on snowfall rates. *J. Appl. Meteorol.* 29, 153–163.
- Newman, A.J., Kucera, P.A., Bliven, L.F., 2009. Presenting the snowflake video imager (SVI). *J. Atmos. Ocean. Technol.* 26, 167–179.
- Notaroš, B.M., Bringi, V.N., Kleinkort, C., Kennedy, P., Huang, G.-J., Thurai, M., Newman, A.J., Bang, W., Lee, G., 2016. Accurate characterization of winter precipitation using multi-angle snowflake camera, visual hull, advanced scattering methods and polarimetric radar. Invited paper, special issue advances in clouds and precipitation. *Atmosphere* 7 (6), 81–111.
- Pruppacher, H.R., Klett, J.D., 1978. *Microphysics of Clouds and Precipitation*. D. Reidel Publishing Company, Boston.
- Ray, S.F., 2002. *Applied Photographic Optics*, 3rd ed. Focal Press, Oxford, pp. 217–220 (ISBN 0-240-51540-4).
- Russ, J.C., 2006. *The Image Processing Handbook*, 5th ed. Florida, CRC Press, Boca Raton (ISBN 0-8493-7254-2).
- Ryzhkov, A.V., Zrnić, D.S., Gordon, B.A., 1998. Polarimetric method for ice water content determination. *J. Appl. Meteorol.* 37, 125–134.
- Schönhuber, M., Urban, H.E., Randeu, W.L., Poiars Baptista, J.P.V., 2000. Empirical relationships between shape, water content and fall velocity of snowflakes. In: *ESA SP-444 Proceedings, Millennium Conference on Antennas & Propagation*, April 9–14, 2000, Davos, Switzerland.
- Sekhon, R.S., Srivastava, R.C., 1970. Snow size spectra and radar reflectivity. *J. Atmos. Sci.* 27, 299–307.
- Sobel, I., 1970. *Camera models and Machine Perception*. Ph. D Dissertation Artificial Intelligence Lab. Stanford University (AIM-21).